Quantification of Errors in Applying DIC to Fiber Networks Imaged by Confocal Microscopy

M. Sarkar, J. Notbohm[*]

Department of Engineering Physics, University of Wisconsin–Madison, Madison, WI, USA

[*] Correspondence to:

Jacob Notbohm

Department of Engineering Physics

University of Wisconsin–Madison

jknotbohm@wisc.edu

525 Engineering Research Building

1500 Engineering Drive

Madison, WI, 53076, USA

+1.608.890.0030

Keywords

Abstract

Background: An assumption of Digital Image Correlation (DIC) is that the displacement field within each subset is relatively smooth, captured with reasonable accuracy by, for example, linear or quadratic shape functions. Although this assumption works well for many materials, it becomes problematic for heterogeneous materials, such as fiber networks, wherein the length scale of heterogeneity matches the size of a subset. **Objective:** Here we applied DIC to fibrous networks made of collagen, for which displacements at the scale of a subset are highly heterogeneous, but errors caused by the heterogeneity are difficult to quantify. We developed a method to quantify such errors. **Methods:** We began by generating a synthetic three-dimensional fiber network with structure matching that of gels made of fibrous collagen. We then formulated an algorithm to mimic the way in which a confocal microscope images the fibers at its focal plane, thereby generating synthetic images similar to those obtained in experiments. Displacement boundary conditions were applied to the synthetic fiber networks, and the resulting displacement fields were computed using a finite element solver. DIC was applied to the synthetic images, and displacements were compared to the data from the finite element method, enabling rigorous quantification of error. **Results:** Point-wise errors in the DIC-measured displacements were substantial, often exceeding 40%, but over regions far larger than the length scales of heterogeneity or the DIC subset size, errors were modest, *e.g.*, $\leq 15\%$. **Conclusions:** Although DIC can accurately measure displacements of fiber networks at length scales larger than the subset window, quantification of mechanical behavior at the scale of material heterogeneity will require new methods to complement or replace the use of DIC.

Introduction

Digital Image Correlation (DIC) and Digital Volume Correlation (DVC) use random patterns on or within the test specimen as a messenger of deformation data [1]. The random patterns, often referred to as speckle patterns, create distributions of intensity, which control the accuracy of these techniques. To ensure sufficient information is contained, it is common to deposit artificial speckle patterns on the surface of the specimen prior to imaging. Whereas application of the speckle pattern and use of DIC is straightforward for homogeneous materials, care must be exercised when studying heterogeneous materials, for which accurately capturing the heterogeneous deformations requires that the length scale of the speckles be smaller than the length scale of the material heterogeneity. This separation of scales ensures that the DIC algorithm's built-in shape functions accurately match the true deformations undergone by the material. Mismatch causes interpolation bias, which, in addition to correlation noise, is a major source of error in DIC measurements [2]. Using artificially generated speckles, it is often possible to achieve separation of scales, and DIC has successfully been applied to numerous heterogeneous materials, such as fiber-reinforced composites [3], gels [4], foams [5], concrete [6], polycrystals [7], and soils [8].

However, there are numerous instances in which it is challenging or impractical to add a customized speckle pattern to the specimen. Examples include microcomputed X-ray tomographic images of bone [9–11], confocal microscope images of fibrous materials [12–17], and satellite images of the earth's surface [18–20]. In these examples, the user must rely on natural texture, resulting from, for example, heterogeneous microstructure or random topography. The natural texture is sometimes referred to as natural speckles. There exist two major concerns that can increase the measurement error. Firstly, with natural speckles, the user has less control over the distribution of intensity. Secondly, in contrast to artificial speckles, natural speckles exist on the same length scale as heterogeneity within the material. While the first concern can often be mitigated by altering the imaging settings, the second always persists. Moreover, when using natural speckles, it is common for the desired spatial resolution to match the length scale of material heterogeneity, which could further enhance measurement errors [21]. There is no established method to quantify these errors.

Here, we developed a method to quantify errors associated with use of DIC on images of a highly heterogeneous material. The material chosen was a network of fibers made of collagen, with the individual fibers themselves serving as the random high contrast speckle pattern. The length scale of the material heterogeneity, the fibers, is comparable to the desired spatial resolution, making the application of DIC to this type of material subject to the errors described above. A further complication is that these fibrous materials also exhibit local heterogeneities in stiffness that renders the displacement field to be nonaffine, *i.e.*, deviating from the case of uniform strain [22]. Several numerical models of fiber networks have reported nonaffine displacements by considering each fiber as a beam that resists both lateral
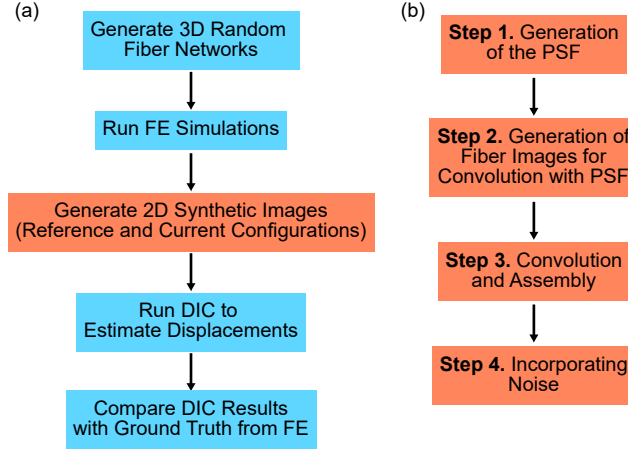
Figure 1: (a) Flowchart of the overall method. (b) Flowchart of algorithm to generate synthetic images.

bending and axial stretching [23–27]. Since fibers in collagen networks are slender, the dimensionless ratio of stiffness in bending to stretching is small, typically on the order of 10^{-4} [28–31]. As a result, the mechanics are dominated by fiber bending, which, due to randomness of the fiber network, causes the displacement field to be highly heterogeneous on the length scale of the fibers. Experiments have corroborated these findings by quantifying heterogeneous fiber rotations [32] and displacements [33–36]. The local heterogeneity causes the deformation field to differ strongly from the shape functions built into the DIC algorithm, which could generate appreciable errors [21, 37]. It remains difficult to quantify these errors, because the true displacement field is typically unknown. Inspired by a workflow proposed in ref. [38], we quantified errors by applying DIC to simulated (synthetic) images for which the ground-truth displacement fields were known. We started by creating an algorithm to generate synthetic images from a numerical three-dimensional (3D) model. These images resembled those captured by a confocal microscope on gels made of collagen fibers. Finite element (FE) software was used to apply displacement boundary conditions to the model and to solve for the deformed state. For both the reference and deformed states, we generated the corresponding synthetic images, and correlated them using DIC. The results were then compared with the FE data, enabling precise quantification of errors

Methods

A summary of our methodology is shown in Fig. 1a. In brief, we created synthetic 3D models of fiber networks and used FE software to deform them under realistic loading conditions. Synthetic images were generated from the fiber networks before and after deformation, allowing for the use of DIC to estimate the displacements. Comparison between the data from FE and the estimated data from DIC enabled quantification of errors. Below, we elaborate on each step.

4

Confocal Microscopy

We began by imaging gels made of fibrous collagen. We neutralized acidified rat tail collagen type I (Corning) with a buffer and added a fluorescent dye. Then we polymerized that mixture at 22°C to obtain a matrix of labelled collagen fibers. We prepared collagen matrices at a concentration 2 mg/mL. Full details are given in our prior study [17].

The collagen matrices were imaged with a spinning disk confocal microscope (Yokogawa CSU-X1) having pinholes of diameter 50 μm. The spinning disk system was attached to a Ti-E base (Nikon). Images were acquired with a 20× 0.75 NA air objective (Nikon) and a Zyla sCMOS camera (Andor). The system was run with IQ3 acquisition software (Andor).

Generation of Synthetic Random 3D Fiber Networks

We generated synthetic 3D random fiber networks with tunable fiber length and nodal density using a previously developed algorithm [27] that uses a simulated annealing-based technique, originally proposed elsewhere [39, 40], to achieve desired distributions of fiber length (defined as the distance between nodes corresponding to the endpoints of each fiber) and connectivity (defined as the number of fibers meeting at each node). In brief, the algorithm deposits nodes in space, connects them with fibers, and then moves the nodes and swaps fibers between different nodes until the desired average fiber length, alignment, and connectivity is achieved. This algorithm can generate networks with domain dimensions and average fiber lengths at any length scale. The algorithm is available online in a public repository at the link in the Code Availability statement.

For this study, we generated random fiber networks that matched the images of the collagen gels. The average fiber length L_f was chosen to be 20 and 30 μm, which matches previously reported fiber lengths in collagen gels prepared under similar conditions [36]. For each value of fiber length, we generated two networks each having a value of nodal density (nodes/volume), 0.01 and 0.025 nodes/μm^3, which qualitatively matched the densities of the imaged collagen gels. Thus, there were four different fiber networks as summarized in Table 1. Fiber networks generated by this algorithm had a tendency to deposit more nodes near domain edges causing non-uniformity in nodal density, so nodes near the edges were cropped out. After cropping, the in-plane (x and y) dimensions, L_x and L_y, were each chosen to be 245 μm, which matches the dimensions of images acquired by the confocal microscope. The out-of-plane (z) dimension, L_z, was chosen to be 5 μm to reduce the computational time required for network generation and subsequent FE calculations.

Network	L_f (µm)	Nodal density (nodes/µm^3)
A	20	0.01
B	30	0.01
C	20	0.025
D	30	0.025

Table 1: Details of the four different synthetic networks generated to mimic collagen gels.

Finite Element Simulations

On each network, we imposed several different displacement boundary conditions by performing 3D FE simulations using the commercially available FE software Abaqus (Dassault Systèmes). Each fiber was modeled as a three-noded quadratic beam element, and connections between fibers were welded such that they transmitted both forces and moments. During loading, fiber networks exhibit nonlinearity, which results primarily from geometric changes associated with displacement and realignment of fibers rather than inherent nonlinearity of the individual fibers [41, 42]. Hence for the sake of simplicity, we assumed each fiber to be linear and elastic.

As network deformations were large, we used the Newton-Raphson based quasi-static solver, as in our prior work [43]. As this solver is unable to converge to a static equilibrium for very large geometric nonlinearities [44], we divided the full applied displacement boundary condition into multiple equally spaced load steps, finding 20 steps to be sufficient. The use of 20 steps reduced the convergence error but did not eliminate it. However, because this work used only the FE results for DIC, and because DIC quantifies only the kinematics, our study required only that the computed displacement fields be kinematically compatible, which is ensured regardless of whether perfect force equilibrium was achieved.

Generation of Synthetic Images

Here we describe our procedure to generate synthetic images of the fiber network before and after undergoing deformations imposed by the FE solver. We mimicked imaging of collagen gels by confocal microscopy, in which image features at the focal plane of the specimen are convolved with the point spread function (PSF), which is defined as the image created by a point source of light. We formulated an algorithm to simulate such imaging, as described in the following four steps and summarized in Fig. 1b. Code to run the algorithm is available in a public repository at the link in the Code Availability statement.

Step 1: Generation of the PSF

We began by noting that a confocal microscope produces a two-dimensional (2D) image by sampling the 3D space, where the thickness of the image in the out-of-plane (z) direction depends on the PSF. The theoretical intensity I of

the PSF of a confocal microscope having pinhole size smaller than the resolution limit is given by [45, 46]

$$I(\tilde{z}, \tilde{r}) = \left(\frac{2}{\tilde{z}}\right)^4 \left[U_1^2(\tilde{z}, \tilde{r}) + U_2^2(\tilde{z}, \tilde{r})\right]^2 I_0,$$

(1)

where I_0 is the peak intensity at the focal point, U_1 and U_2 are Lommel functions of order 1 and 2, respectively, and $\tilde{z}$ and $\tilde{r}$ are dimensionless spatial parameters,

$$\tilde{z} = \frac{2\pi}{\lambda} \frac{NA^2}{n} z \quad \text{and} \quad \tilde{r} = \frac{2\pi}{\lambda} NA \sqrt{x^2 + y^2},$$

(2)

with NA being the numerical aperture of microscope, λ being the wavelength of light, n being the refractive index of the immersion medium (air, water, or oil) between the specimen and objective, and x, y and z being spatial coordinates where the image is acquired in the x–y plane. A Lommel function of order n is defined as

$$U_n(\tilde{z}, \tilde{r}) = \sum_{s=0}^{\infty} (-1)^s \left(\frac{\tilde{z}}{\tilde{r}}\right)^{n+2s} J_{n+2s}(\tilde{r}),$$

(3)

where $J_{n+2s}(\tilde{r})$ is the Bessel function of the first kind of order $(n+2s)$. Plots of the PSF are shown in Fig. 2a–b.

The parameters matching the imaging of the collagen gels were $n = 1$, $\lambda = 0.525$ μm, and $NA = 0.75$, though in creating the synthetic images we also considered $NA = 0.65$ and $NA = 0.7$ to account for reduced resolution caused by using a pinhole larger than the width of the PSF, which is typical in confocal microscopy, because a small pinhole allows too little light through, requiring the user to increase either the imaging time or the illumination power, both of which can cause photobleaching. Hence, confocal microscopes typically use a pinhole larger than the width of the PSF, and in our case, the pinhole diameter was 50 μm.

Step 2: Generation of Fiber Images for Convolution with PSF

With the PSF established, the next step was to convolve the 3D PSF with a 3D image of the synthetic fiber network. To reduce computation time, the 3D convolution was approximated by a series of 2D convolutions (Fig. 2c); this approximation has been studied in detail in the use of convolutional neural networks [47]. The 2D convolutions were performed on synthetic images containing all fibers within a range of $\tilde{z}$ positions. The ranges of $\tilde{z}$ positions were defined by limiting positions, chosen such that at location $\tilde{r} = 0$, the intensity of the PSF was 90%, 60%, 30%, and 0% of its maximum value. The corresponding dimensionless positions were $\tilde{z} = \pm 1.58$, ± 3.46, ± 5.22, ± 10.03, which, using our imaging parameters, corresponded to $z = \pm 0.27$, ± 0.59, ± 0.89, and ± 1.71 μm. We then used our simulated fiber networks to create synthetic images containing all fibers within the ranges defined by each sequential pair of limiting positions (Fig. 2d). The images had an in-plane pixel size of 0.325 μm, which matched the experimental images. Each image was assigned a z position matching the center of the z range used to generate that image, with
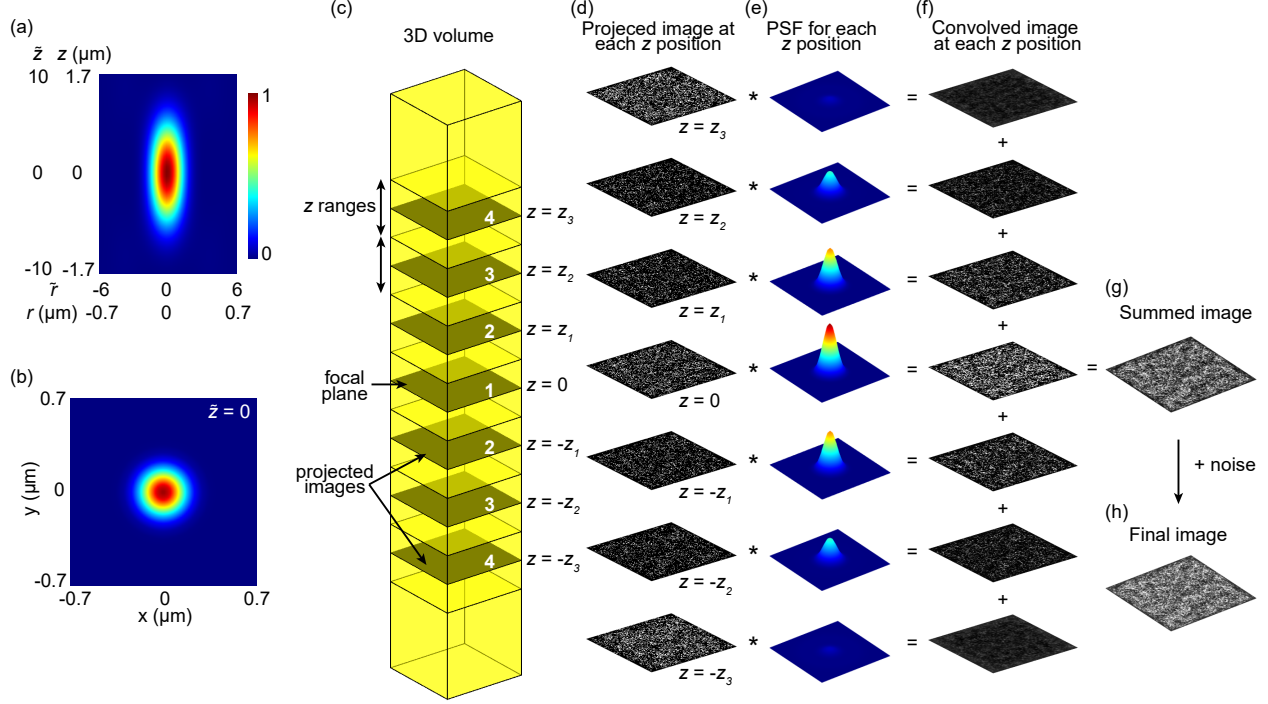
Figure 2: Generation of synthetic images mimicking confocal imaging. (a) PSF in $\bar{r}$-$\bar{z}$ coordinates. Units in µm result from the choice of parameters to match the experimental images as described in the text. (b) PSF in x-y (in-plane) coordinates at position $\bar{z} = 0$. (c) Schematic of a 3D volume imaged by a confocal microscope. All fibers within each z range shown were used to create an image at planes identified by $z = 0$, $\pm z_1$, $\pm z_2$, and $\pm z_3$, which correspond to $z = 0$, ± 0.43, ± 0.74, and ± 1.30 µm, respectively. (d) Resulting projected images at each z position. (e) In-plane PSF at each z position. (f) Each projected image was convolved with the corresponding PSF, resulting in a set of convolved images. (g) The images were summed. (h) Noise was added to produce the final image.

values corresponding to $z = 0$, ± 0.43, ± 0.74, and ± 1.30 µm. Eq. 1 was evaluated at each of these positions to evaluate the PSF corresponding to each image (Fig. 2e). As shown in the figure, the PSF at the top and bottom locations chosen, $z = \pm 1.30$ µm, was nearly zero, indicating that the range of z chosen spanned the PSF.

Step 3: Convolution and Assembly

A 2D convolution between each projected image (Fig. 2d) and its corresponding PSF (Fig. 2e) was performed. The resulting seven convolved images (Fig. 2f) were added to obtain the final image (Fig. 2g).

Step 4: Incorporating Noise

As images acquired by a confocal microscope contain noise resulting from numerous sources [48], we added noise to the synthetic images. To determine the appropriate distribution of noise to use, we analyzed our experimental images of collagen gels. For each image, we manually identified regions between fibers and plotted histograms of the intensities. As the intensity in regions between fibers would be zero in the absence of noise, the resulting histograms approximated the distribution of noise. We typically observed these distributions to be Gaussian with mean and standard deviation 35.94% and 16.42%, respectively, of the median intensity of the image. Therefore, we added a random variable drawn from this measured distribution to each pixel of the synthetic images to represent the imaging

noise (Fig. 2h).

Customizability of Image Generator Algorithm

It is possible to customize our image generator algorithm to suit imaging techniques different from confocal microscopy. For example, one could alter the built-in 3D PSF in Step 1 using a PSF appropriate for X-ray micro-computed tomography (*e.g.*, ref. [49]) to prepare synthetic tomograms mimicking X-ray micro-computed tomography (similar to refs. [50] and [51]), which are often needed to validate the accuracy of image analysis algorithms. As another example, by using an appropriate 2D PSF in Step 1 and removing the "assembly" feature in Step 3, it is possible to produce synthetic telescopic observations of astronomical objects similar to ref. [52]. Our algorithm could also be used in more general situations of applying DIC on images of 2D samples, but in such situations, the smallest image feature is typically larger than the width of the PSF, meaning convolution with the PSF would not be essential. Instead, one could include considerations that are relevant in other imaging systems, such as uneven illumination as in ref. [53].

DIC Algorithms Used

The DIC algorithm used in the majority of this study was the local algorithm Fast Iterative Digital Image Correlation (FIDIC) [54], which is the same algorithm used in our prior publications on fibrous materials [17, 36, 43, 55]. Where stated in the Results section, we also used a global algorithm, Augmented Lagrangian Digital Image Correlation (ALDIC), which enforces displacement compatibility and strain smoothness across subsets [56]. The subset size used in the correlations varied from 16×16 to 64×64 px (5.2×5.2 to 20.8×20.8 μm^2) and is reported in the Results. The subset spacing was a quarter of the subset size. In some cases, the magnitude of local deformation of speckle features (*i.e.*, of the fibers) within each DIC subset between the first and last load step of the FE solver was too large for correlation by DIC. For this reason, we applied the DIC incrementally to pairs of images from sequential load steps and computed the total nodal displacements by summing the incremental nodal displacements.

Interpolating FE Data onto a Grid for Comparison to DIC Results

The displacement at each node of the fiber network, computed by the FE solver, were used for comparison against the results of DIC. As displacements computed by DIC were on an uniform grid, the FE data was interpolated to the same grid using natural interpolation, which is C^1 continuous. Given that DIC correlates subsets of finite size, it also spatially smooths the data. Hence, the FE data was smoothed as well, with the method of smoothing designed to match as well as possible the smoothing performed by the FIDIC and ALDIC algorithms. For FIDIC, the algorithm multiplied each image subset by a weight function designed to increase the spatial resolution of the correlation while
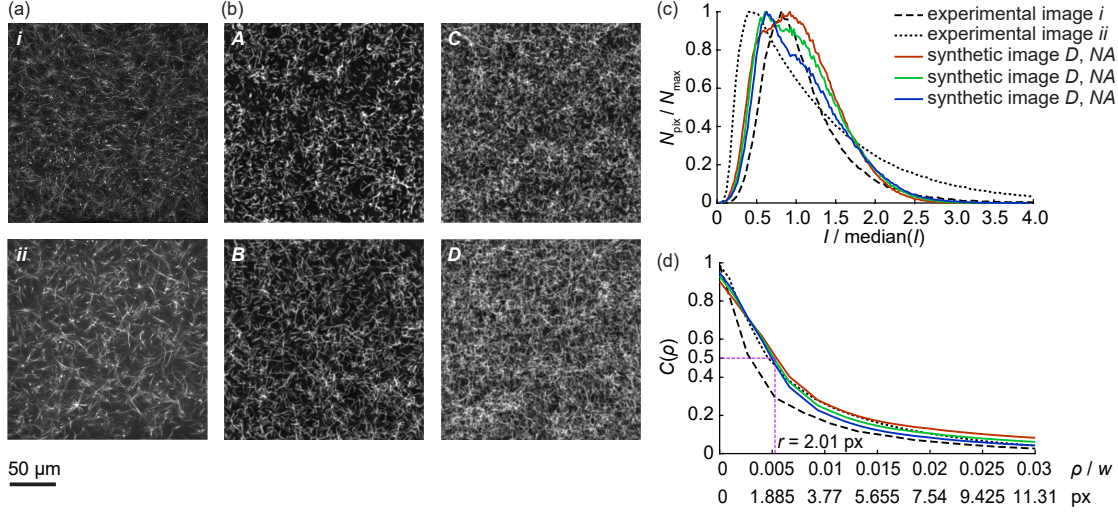
9

Figure 3: Qualitative and quantitative comparison of experimental and synthetic images. (a) Images of 2 mg/mL collagen gels from confocal imaging. (b) Synthetic images generated by our algorithm. Fiber length and nodal density are identified by *A*, *B*, *C*, & *D* as defined in Table 1. (c) Histograms of image intensity *I* for experimental images and synthetic images of network *D* generated with different values of numerical aperture. Curves are normalized by dividing the number of pixels in each bin (N_{pix}) by the maximum value (N_{max}). (d) Autocorrelation of intensity as a function of both normalized distance ρ/w (where w is the width of the image) and distance in pixels. The autocorrelation radius, $r = 2.01$ px, is defined to be the distance at which $C = 1/2$ and is an indicator of the effective speckle size in the synthetic image.

minimizing noise [57]. Therefore, for comparison between FIDIC and FE data, we smoothed the interpolated FE data using this same weighing function. ALDIC, however, did not apply a weight to each image subset, so for comparison to ALDIC results, the FE data was averaged over a square window the same size as the subset used for ALDIC.

Results and Discussion

Quality Assessment of Synthetic Images

Representative experimental images of density 2 mg/mL are shown in Fig. 3a, with representative synthetic images of different density and fiber length shown in Fig. 3b. Qualitative comparison between the experimental and synthetic images shows that fiber lengths, widths, and densities appear to match well. A more quantitative comparison between synthetic and experimental images was performed by plotting histograms of intensities for synthetic and experimental images. For parity in comparison, we normalised the intensity (*I*) of each image with the median intensity of that image. The number of pixels in each histogram bin, N_{pix}, was normalized by the maximum number of pixels in any bin, N_{max}, of the corresponding image. The synthetic image of network *D* was found to match the experimental images the best and was used to create the histograms (Fig. 3c). Synthetic images generated with *NA* equal to 0.65 and 0.70 gave a slightly better match to the experimental images than the synthetic image generated with *NA* of 0.75 (Fig. 3c).

For a second quantitative comparison between synthetic and experimental images, we used the spatial autocorre-

lation, C, defined as

$$C(i,j) = \frac{< (I(m,n) - \mu_I)(I(m+i,n+j) - \mu_I) >}{\sigma_I^2}, \tag{4}$$

where I is the image intensity, the index pairs (m,n) and (i,j) indicate the rows and columns corresponding to each pixel in the image, μ_I and σ_I are, respectively, the mean and standard deviation of image intensity, and the angle brackets $(<>)$ denote a mean over all pixels identified by m and n. The 2D autocorrelation $C(i,j)$ was averaged over circles of different radii ρ centered at $(i = 0, j = 0)$. The autocorrelation was computed for both the experimental images and synthetic images of network D with NA equal to 0.65, 0.70, and 0.75 (Fig. 3d). The variation of the auto-correlation between the synthetic images created with different NA was minor, and all autocorrelations compared well with the experimental images, indicating that spatial variation in image intensity matched between the experimental and synthetic images. The NA of the objective (0.75 in our experiments) should be thought of as an upper bound, and the resolution achieved in our experiments was reduced slightly by the fact that the pinhole size used was larger than the size of the PSF as described in the methods. Considering that the specific choice of NA did not have a major effect on the results and the value of 0.75 was an upper limit, we chose to use a slightly reduced value, $NA = 0.70$, to generate the synthetic images for the remainder of our study.

As the autocorrelation quantifies how the intensity changes over distance, we also used it to estimate the effective speckle size, which we defined by the radial distance r at which the autocorrelation function decreased to a value of 1/2. In the synthetic images of network D, the average autocorrelation radius had a value of 2.01 px (Fig. 3d). This number is close to the recommend size of 2.2 px for DIC, as suggested in ref. [58]. Additionally, given that the subsets used in our analysis were $\geq 16 \times 16$ px, the effective speckle size of 2.01 px implies that each subset had far greater than three speckles, which is commonly considered to be the minimum number of speckles for each subset [59].

Noise Floor and Rigid Body Translation

Our first use of DIC was to quantify the noise floor. Two networks were chosen, corresponding to the sparsest (A) and densest (D). For each network, two images were generated in the undeformed state and, hence, differed only by the added noise. The images were correlated by FIDIC to give the noise floor, which was random (Fig. 4a), with histograms showing the distribution of noise to resemble a Gaussian distribution (Fig. 4b).

Next, we performed rigid body translations in the x and y directions of magnitude 2.5 μm, which was a typical magnitude of displacement undergone by the fiber networks under applied loadings referred to "intermediate" in the subsequent sections. Edge effects, caused by DIC subsets moving out of the field of view, were eliminated by removing them from the data set. Representative maps of displacements in the x and y directions (u and v, respectively) indicated a slight systematic underestimate of the applied displacement (Fig. 4c). Histograms confirmed the underestimate, with the typical value of average error being -0.6% and standard deviation of error being 0.005% for both u and v in
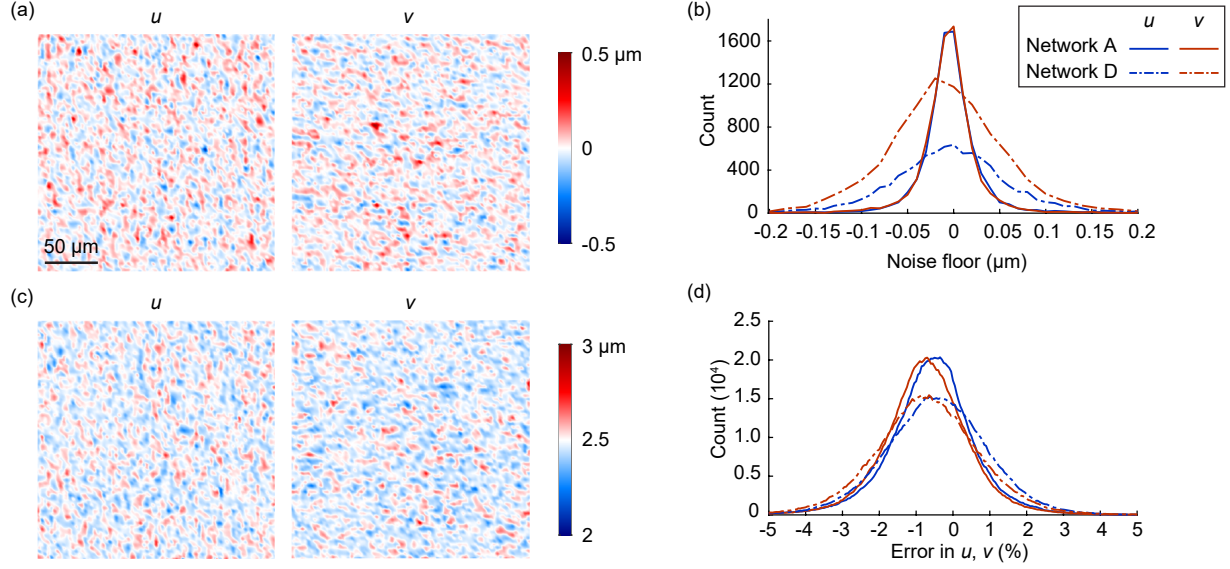
11

Figure 4: Verification of DIC on synthetic images. (a) Noise floor computed by correlating a pair of undeformed images. Results show u and v, the components of displacement in the x and y directions, for network D. (b) Histogram showing distribution of noise for networks A and D. (c) Displacements computed after applying rigid body translation of 2.5 µm in both the x and y directions to network D. (d) Distribution of errors of DIC in quantifying displacements of the 2.5 µm rigid body translation for networks A and D. For all results in this figure, DIC was run with a subset size of 32×32 px and subset spacing of 8 px.

networks A and D (Fig. 4d).

Errors Under Uniform Boundary Conditions

The first boundary condition studied was simple shear, wherein a subset of nodes at the bottom of the 3D fiber network were fixed and a subset of nodes at the top were translated in the positive x direction. The sizes of the regions for which nodes were fixed or translated were large, which we found to be necessary to avoid strong strain localization and to produce a nominally constant strain field in the center of the image. The regions where nodes were fixed or translated are shaded blue in Fig. 5a. Three different magnitudes of shear strain were applied, low (2.4%), intermediate (23%), and high (66%). Displacements were allowed to occur in the z direction for all nodes within ± 0.25 µm of the focal plane ($z = 0$). As described in the "Methods" section, the translation was applied in 20 load steps in the FE solver, generating 19 intermediate states and one final deformed state. Considering that we were interested in evaluating DIC in a state of simple shear, we defined a region of interest (ROI) (dashed rectangles in Fig. 5a, b) for which the strain was nominally constant. Images of the ROI were generated corresponding to each load step, and the sequence of images was correlated by DIC.

Representative images of the reference and final states are shown for intermediate shear strain (23%) in Fig. 5a–b. These images correspond to fiber network C, which we selected to use due to it having intermediate values of nodal density and fiber length. To observe the deformations during intermediate load steps, we also show a series of five images of the ROI (Fig. 5c), labeled i–v, where i and v are, respectively, the reference and final states, and ii–iv
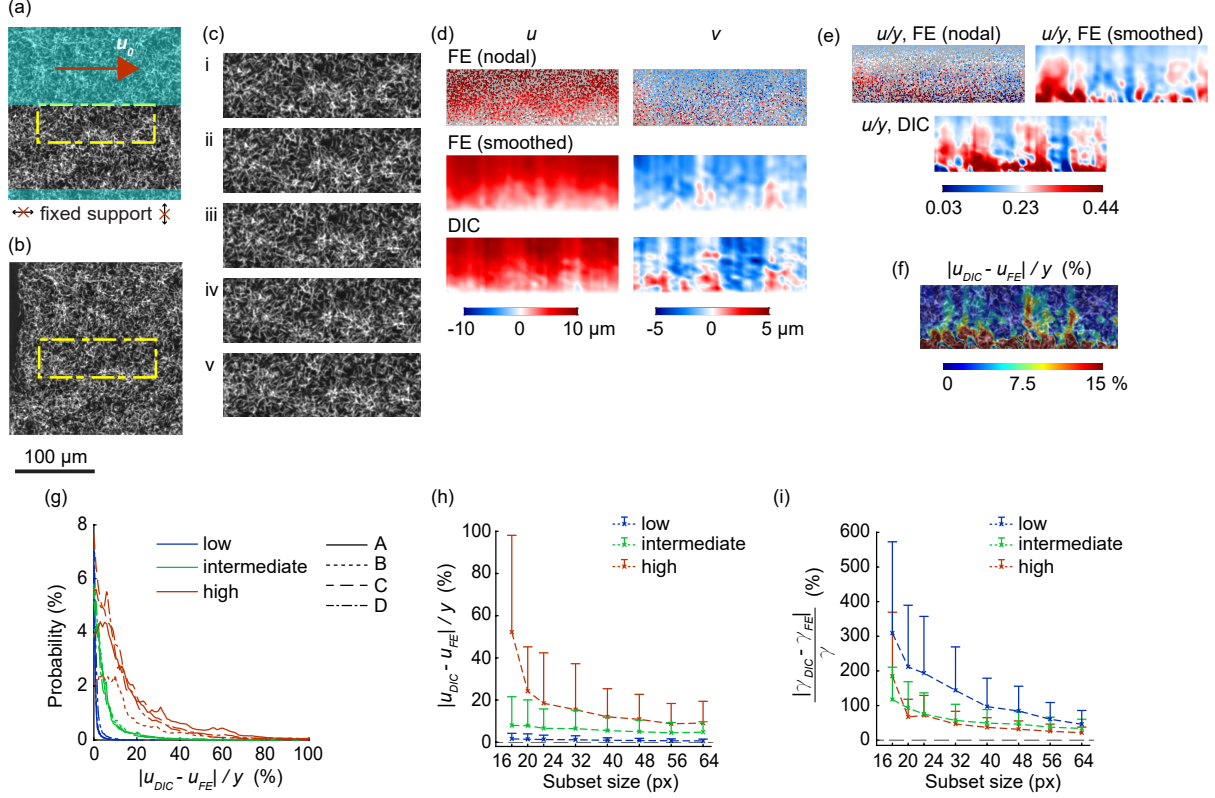
12

Figure 5: Deformation in simple shear. (a) Boundary conditions used. The bottom of the network was fixed, and top of the network was translated in the positive *x* direction in simple shear. Fixed and translated nodes are highlighted in blue. Results were analyzed in the ROI defined by the yellow rectangle. (b) Image of deformed fiber network under 23% (intermediate) shear strain in the ROI. (c) Series of images showing the ROI at different nominal strains, with *i* being undeformed and *v* being the image corresponding to 23% strain. (d) Maps of displacements *u* and *v* in the ROI at intermediate strain showing the field of nodal displacements from FE, the smoothed FE results used for comparing to DIC, and the DIC results. (e) Maps of normalized displacement (u/y) in the ROI showing original FE nodal, smoothed FE, and DIC results. (f) Map of absolute point-wise error in normalized displacement (u/y) in smoothed FE and DIC results. (g) Distribution of errors in DIC estimates of normalized displacement (u/y) for three levels of applied strain (low, 2.4%; intermediate, 23%; and high, 66%) and all four synthetic fiber networks. In panels d–g, DIC used a subset size of 32×32 px and subset spacing of 8 px. (h) Errors in DIC estimates of normalized displacement for varying subset sizes at small (2.4%), intermediate (23%) and high (66%) magnitudes of applied strain. (i) Errors in DIC estimates of local strain, normalized by the applied strain (γ), for varying subset sizes at low (2.4%), intermediate (23%) and high (66%) magnitudes of applied strain. The DIC subset spacing was a quarter of the subset size for all cases. Black dashed line indicates zero in panels h and i. Data in panels a–f, h and i are from network *C*.

correspond to load steps 5, 10, and 15. A map of the total nodal displacements from the FE results (Fig. 5d) showed a gradient of *u* over distance *y* along with strong fluctuations over space. Because DIC spatially filters the data, we smoothed the data using a filtering scheme that matched the DIC as described in the Methods section, which gave a displacement field that was smoother, yet still exhibited spatial fluctuations (Fig. 5d). Displacements computed by DIC similarly showed a clear gradient in *u* over *y* with fluctuations having similar spatial frequency as the smoothed FE data.

As a simple measure of the normalized displacement, we computed the quantity u/y, with both *u* and *y* defined to be zero at the bottom of the ROI. Qualitative comparison of u/y between the smoothed FE and DIC data showed regions of high and low strains matched reasonably well (Fig. 5e). Careful comparison between the FE and DIC data,

13

however, showed that at some locations, large differences were present. To quantify these differences, we computed the error in the DIC measurement of displacement, by taking the absolute value of the point-wise difference between the DIC measurement and the smoothed FE data (Fig. 5f). Errors were computed for different levels of strain (low, intermediate, and high) and all four fiber networks (A, B, C, and D). The distributions of point-wise errors appeared to be approximately half-normal (Fig. 5g), with the mean errors typically near zero. For intermediate and high magnitudes of strain and all networks, the errors were large, with standard deviations in the tens of percent. To determine whether the large standard deviations resulted from the size of subset used for DIC, we repeated the DIC with subset sizes ranging from 16×16 to 64×64 px (5.2×5.2 to 20.8×20.8 μm^2) (Fig. 5h). For the different subset sizes, the magnitudes of mean error were typically small ($\leq 15\%$) except at the smallest subset sizes for which the mean error increased rapidly at high strain ($\approx 52\%$ and 24% at subset sizes of 16×16 and 20×20 px), possibly caused by noise that typically occurs when using small subsets in DIC. The standard deviations of errors decreased with increasing subset size, at the cost of increased spatial smoothing. For all subset sizes, for intermediate and high strains, the sums of mean and standard deviation of errors were typically between 10 and 40%, indicating large point-wise errors in the DIC with respect to the smoothed FE data. To examine whether these errors were dependent on the image contrast inside each DIC subset, we evaluated contrast by computing the span of the gray scale intensity within each DIC subset and compared it to the error at each subset, but there was negligible correlation between the error and image contrast (Fig. 8 Appendix), suggesting the errors were not related to image quality. We next considered how these errors in displacement would lead to errors in local strain by computing the gradient of displacement field using the Matlab function "gradient." We took the absolute point-wise difference between the local strain data in the DIC and the smoothed FE data and then normalized the result by the applied strain. The mean and standard deviation of these errors depended on subset size (Fig. 5i) in the same way as in the Fig. 5h, but the standard deviation of errors were inversely proportional to the level of applied strain. Given that this error data was normalized by applied strain, both the numerator and denominator changed when applied strain increased, but the denominator (applied strain) had a dominant effect in this case, meaning that the error in the local strain measurement decreased with increasing applied strain.

To determine whether the large point-wise errors in displacement were an artifact of the specific DIC algorithm used, we applied another DIC algorithm, ALDIC, to the images of simple shear and again quantified error at a specific subset size of 32×32 px (Fig. 9, Appendix). Across different strain levels, the magnitudes of mean error were again moderate ($\leq 17\%$), but the sums of the mean and standard deviation of errors were typically between 15–30%, reflecting the existence of large point-wise error in ALDIC as well.

The simple shear boundary condition studied so far was a shape-changing deformation. To assess whether the results were sensitive to other types of deformation, we considered biaxial extension, which changes area (Fig. 10,
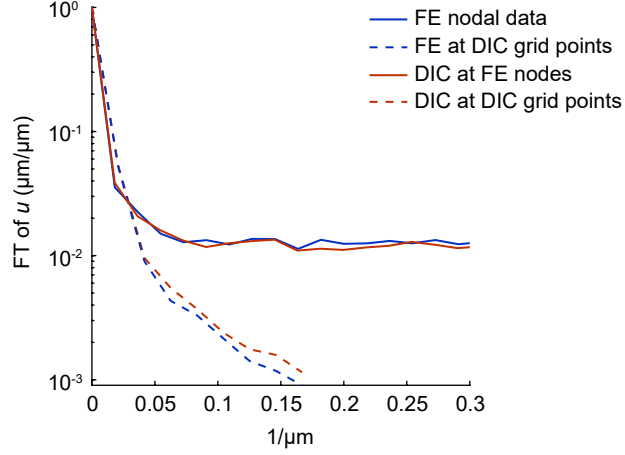
Figure 6: Magnitude of the spatial frequency of displacement field u as quantified by its normalized Fourier Transform (FT). The displacement field u was from simple shear at intermediate strain applied to network C. The solid lines show the FE ground truth nodal data and DIC nodal data, computed by using a subset at each FE node. The dashed lines show the DIC data run with a subset size of 32×32 px and subset spacing of 8 px and the FE data smoothed using the method for averaging that approximates the spatial filter of the FIDIC algorithm, as described in the Methods.

Appendix), and uniaxial extension, which changes both shape and area (Fig. 11, Appendix). For both cases, both mean and standard deviation of errors in the normalized displacements were typically moderate to large, *e.g.*, 15–45%, with their sums often > 50%.

Frequency Content of Displacement Data

So far, our evaluation of DIC has relied on point-wise errors. As another means of evaluating the use of DIC on images of fibrous materials, we questioned how well the spatial frequency content of the DIC results matched that of the ground truth FE data. To this end, we used the results from simple shear (intermediate magnitude) deformation of network C and computed the Fourier transform of the displacement field u from both the FE and DIC data. The Fourier transformed data was averaged over angle, its absolute value was taken, and it was normalized by its maximum value, hence giving a graph of the normalized Fourier transformed data against spatial frequency (Fig. 6). The data from FE exhibited a peak at the smallest wave numbers, with a plateau at intermediate and large wave numbers, indicating spatial fluctuations over a broad range of wave numbers.

Upon smoothing and interpolating the FE data onto the grids used for comparison to the gridded DIC data, the plateau disappeared, with the curves corresponding to the smoothed data being notably lower than the unsmoothed, ground truth data, especially for wave numbers greater than ≈ 0.03 μm^{-1}, *i.e.*, for length scales smaller than ≈ 33 μm. Results from gridded DIC matched reasonably closely to the smoothed FE data, consistent with the well-known fact that DIC acts as a spatial filter. Hence, DIC would be unable to resolve accurately changes in displacements occurring over distances $\lesssim 33$ μm. To investigate if this loss in spatial content could be attenuated, we evaluated the DIC displacement field directly on each FE node by using a DIC subset centered on the pixel corresponding to that FE

15

node. Although the resulting nodal DIC data appeared to mitigate the loss of spatial content, a point-wise comparison of displacements between the unsmoothed FE data and the DIC data at FE nodes exhibited large errors (mean 13.9% and standard deviation 31.3%), indicating the nodal DIC data for wave numbers $\gtrsim 0.03$ μm^{-1} contained substantial white noise. This again highlights the limitation of DIC in resolving displacements over distances $\lesssim 33$ μm. It is further interesting to note that the comparison of gridded DIC with smoothed FE revealed reduced point-wise errors (mean 6.5% and standard deviation 8.7%), due to the spatial smoothing of displacement fields.

Contracting Cylindrical Inclusion Boundary Condition

Although errors may be large when applying DIC to our images on length scales smaller than 33 μm, it may be that at larger length scales, errors would be tolerable. Such a situation was present in the data on point-wise error, wherein the sums of means and standard deviations were large, but means were frequently $\leq 15\%$, implying that if one computed an average over the entire ROI of the displacement computed from DIC, the result would be reasonably accurate. We sought to test the limits of this idea using a different boundary condition and a metric of the displacement field other than the normalized displacement field used so far. In prior work, we applied DIC to a contracting sphere in a gel of collagen fibers, quantifying the decay of displacements away from the sphere as a means of studying nonlinearity, heterogeneity, and anisotropy of the fiber network [17, 36, 43, 55]. To simulate these conditions, we used a simplified case of a contracting cylindrical inclusion of diameter 60 μm at the center of fiber network C, which had dimensions $245 \times 245 \times 5$ μm^3. Nodes present at the periphery of the inclusion (indicated by dashed circle in Fig. 7a, b) were displaced radially inward to produce 30% contractile strain of the inclusion. As in the simulations of simple shear, the FE model was solved using 20 load steps, and displacements were allowed to occur in the z direction for all nodes within $z = \pm 0.25$ μm across the focal plane ($z = 0$).

The computed nodal displacement field exhibited large fluctuations superimposed over a displacement field that decayed over distance from the contracting inclusion (Fig. 7c). DIC results, using either FIDIC or ALDIC, showed similar fields of displacements, though with far less spatial fluctuation, resulting from the spatial filtering of DIC (Fig. 7d, e). To analyze the decay of displacements over distance, we plotted the inward radial displacement u_r of each node against its radial position r (Fig. 7f). As in our prior work [17, 36, 43, 55, 60], we fitted the displacements to a function of the form $u_r \sim r^{-n}$, with n quantifying the decay of displacements over distance. Given that the simulated boundary conditions were of a contracting cylinder with no variation through the z direction, the solution from linear elasticity is the familiar Lamé problem, for which $n = 1$. In comparison, the fitting gave $n = 0.41$, indicating a long range decay of displacements, which is caused by nonlinearity [17, 27, 60–63]. Fitted values of n from the displacement fields from FIDIC and ALDIC matched closely to the FE data, being 0.42 and 0.43, respectively. Repeating this procedure for a different level of contraction (10% instead of 30%) gave similar results, with a close match of fitted values of n
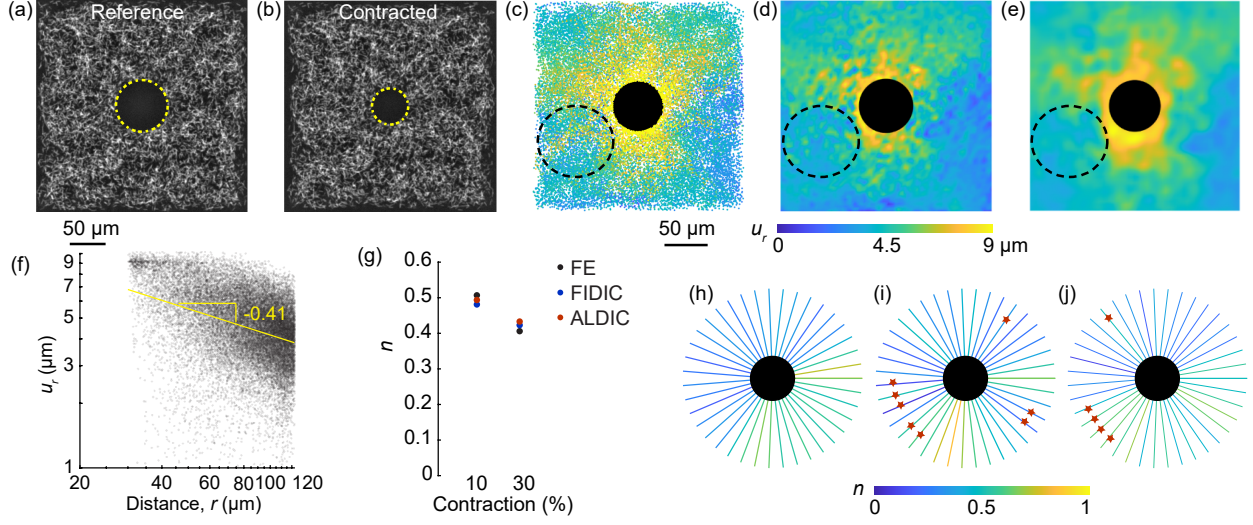
Figure 7: Contracting cylinder boundary condition. (a) Image of 3D network C with central cylindrical inclusion marked by yellow dashed boundary in reference state. (b) Deformed state of the network after 30% contraction of inclusion. (c) Map of radial component of nodal displacement, u_r obtained from FE simulation, with inward defined as positive. (d) Inward radial displacement field measured by FIDIC (subset size, 32×32 px; subset spacing, 8 px). (e) Inward radial displacement field measured by ALDIC (subset size, 33×33 px; subset spacing, 8 px). The black dashed circles in panels c–e identify a region with large spatial fluctuations in the FE displacement field that are not captured in the DIC data. (f) Plot of true (FE) inward radial displacement u_r against radial position r for all nodes on logarithmic axes. The slope of the best fit line indicates $n = 0.41$. (g) Comparison of true and DIC-estimated average displacement decay rates n for 10% and 30% radial contraction. (h) Radial displacements along radial paths drawn outward from the center of the inclusion were fit to $u_r \sim r^{-n}$ using data from all nodes within 2.4 μm of each radial path. Fit powers n are shown by the color of each path. (i, j) Fit powers n for the different radial paths using displacement data computed from FIDIC (i) and ALDIC (j). For each radial path, the error in decay rate n can be assessed by comparing the FE-computed values (h) to the DIC-computed values (i and j). Stars show paths for which the magnitude of the error is $> 50\%$.

between the FE data and the DIC data (Fig. 7g).

To consider how DIC performs compared to the FE data over regions smaller than the entire image, we drew several radial paths outward from the center of the cylinder and performed separate fits for parameter n using displacements of nodes located within a distance of 2.4 μm on either side of each radial path. The results for each path are plotted as a line, with color indicating the value of n. For the FE data (Fig. 7h), all values of n were less than 1, but there was notable variability for paths in different directions due to local anisotropy in fiber network [17]. In comparison, the fitted values of n from the DIC data were also less than 1 and exhibited variability (Fig. 7i–j), but they sometimes differed substantially from the FE data. Paths with substantial error (*i.e.*, $> 50\%$) are indicated by star symbols in Fig. 7i–j. These paths of substantial errors in DIC measurements often appeared to correspond to regions with large spatial fluctuation in the displacement field, as shown by black dashed circles in Fig. 7c–e.. The mean errors of n in the different radial paths were 28% and 27% for FIDIC and ALDIC, respectively.

In summary, DIC was able to accurately quantify a different metric of interest, in this case n, as long as the value of n was computed from a data set corresponding to a sufficiently large region of the image. If the fitted value of n used a smaller data set, such as the data points nearest to a single path in Fig. 7h–j, errors increased substantially, similar to our prior observation of large point-wise errors.

Conclusions

Here we developed a workflow to test the efficacy of DIC on simulated images of fiber networks matching the fibers of a collagen gel. Heterogeneity was caused by the fibrous structure, with the typical fiber length being similar to the desired spatial resolution. The individual fibers served as random high contrast speckles. The DIC measurements exhibited substantial errors (with sums of mean and standard deviation typically $> 40\%$) in a point-wise sense, but the average errors over a sufficiently large region of interest were typically moderate ($\leq 15\%$). Therefore, applying DIC appears to be reasonable in problems that characterize mechanical behavior of fiber networks over a sufficiently large region (*e.g.*, refs. [17, 43, 55]). However, in instances where point-wise displacement data is required, for example, in determining point-wise traction applied by cells within a fibrous matrix, or in characterizing local stiffness of a heterogeneous material, errors in the DIC data are likely to be excessively large. Such situations will require new methodologies to complement or replace DIC. One possible way to address this issue is to complement the mesoscale DIC measurement with a measurement at the microscale, for example, by using a model to account for deformations of the network architecture, *e.g.*, the struts of a cellular material as in ref. [64]. A second possibility could be to develop new methodologies that bypass the DIC displacement measurement step altogether, as has been done in Mechanical Shape Correlation [65], which correlated experimental data of the contour of a deformed structure to corresponding data from an FE simulation. Building on this idea, it could be possible build full-field synthetic images from a model to correlate directly against the experimental images, enabling the model to be improved through iteration. To this end, the workflow described in this manuscript, which used a combination of a model and synthetic images, is a useful starting point.

Acknowledgments

Declarations

Conflicts of Interest Declaration

The authors have no conflicts of interest to declare.

Code Availability

The current versions of the FIDIC and ALDIC code are available from https://github.com/jknotbohm/FIDIC and https://github.com/jyang526843/2D_ALDIC, respectively. The code for mak-

ing the fiber networks and running them in Abaqus is available from https://github.com/jknotbohm/fiber_network_model. The code for making synthetic images mimicking imaging by confocal microscopy is available from https://github.com/jknotbohm/image_generator.

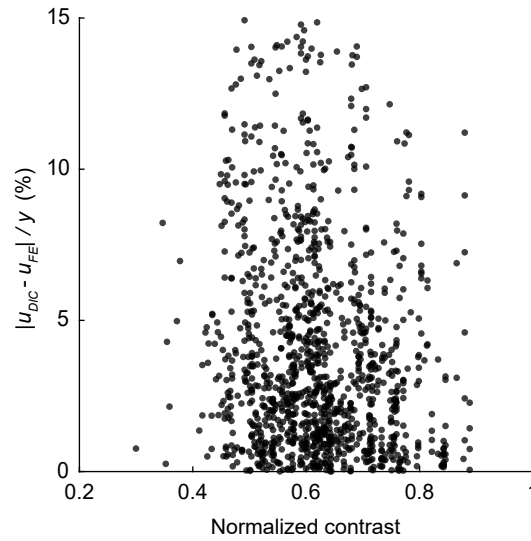# Appendix

The appendix contains Figs. 8–11.

Figure 8: Dependence of error on image contrast. The error shown was from the FIDIC estimates of normalized displacement in the ROI from simple shear at intermediate strain applied to network C. The image contrast inside was calculated for each DIC subset by taking the difference of the maximum and minimum gray scale intensities within each subset and normalizing by the difference between maximum and minimum intensities in the entire image. Each dot corresponds to a different DIC subset. Correlation coefficient, $R = -0.14$. FIDIC was run with a subset size of 32×32 px and subset spacing of 8 px.
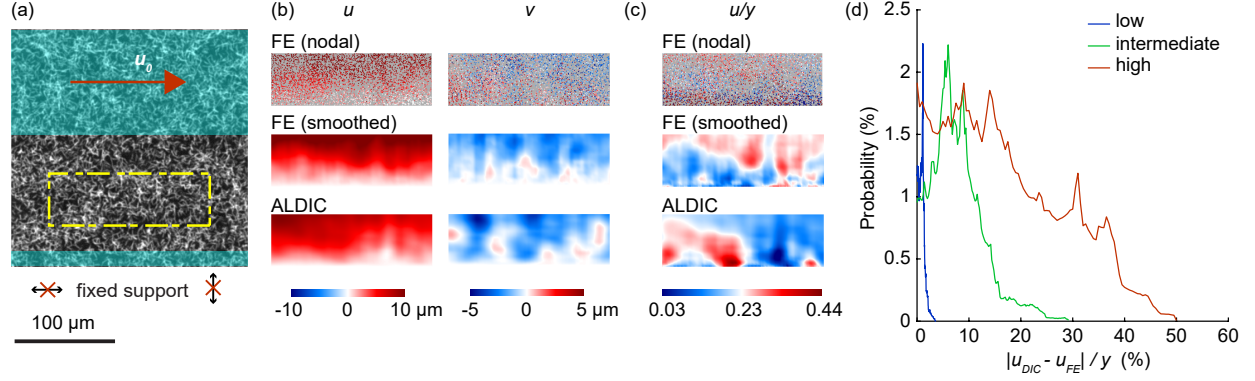
Figure 9: Deformation in simple shear with ALDIC. (a) Boundary conditions used. The bottom of the network was fixed, and the top of the network was translated in the positive x direction. Fixed and translated nodes are highlighted in blue. Results were analyzed in the ROI defined by the yellow rectangle. (b) Maps of displacements u and v in the ROI at intermediate applied strain (23%) showing the field of nodal displacements from FE, the smoothed FE results used for comparing to ALDIC, and the ALDIC results. (c) Maps of normalized displacement (u/y) in the ROI showing FE nodal, smoothed FE, and ALDIC results. (d) Distribution of errors in ALDIC estimates of normalized displacement (u/y) for three levels of applied strain (low, 2.4%; intermediate, 23%; and high, 66%). Network C was used to generate this figure, and ALDIC used a subset size of 33×33 px and subset spacing of 8 px.
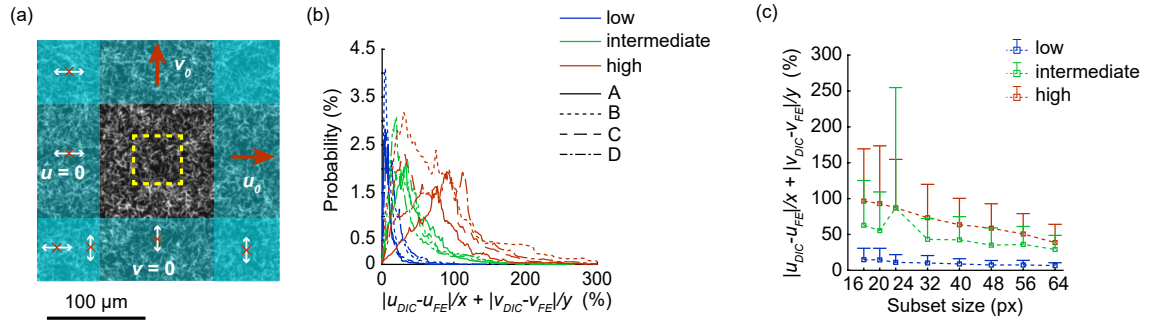

Figure 10: Deformation in biaxial extension. (a) Boundary conditions used. Nodes near the left and bottom sides of the fiber network were constrained to have zero displacement in the x and y directions, respectively. Nodes near the right and top sides of the network were translated in the x and y directions, respectively. The dashed square shows the ROI. (b) Distribution of errors in the ROI in FIDIC estimates of the normalized areal displacement, $u/x + v/y$ (subset size, 32×32 px; subset spacing, 8 px). Colors show levels of applied strain and line types indicate the network being considered. (c) Errors in FIDIC estimates for several different subset sizes at low ($\approx 2\%$), intermediate ($\approx 20\%$) and high ($\approx 60\%$) magnitudes of strain for representative network C. The subset spacing was a quarter of the subset size for all cases.

References

[1] YL Dong and Bing Pan. A review of speckle pattern fabrication and assessment for digital image correlation. *Exp Mech*, 57(8):1161–1181, 2017.

[2] Zeren Gao, Xiaohai Xu, Yong Su, and Qingchuan Zhang. Experimental analysis of image noise and interpolation bias in digital image correlation. *Opt Laser Eng*, 81:46–53, 2016.

[3] Luis Pablo Canal, Carlos González, Jon M Molina-Aldareguía, Javier Segurado, and Javier LLorca. Application of digital image correlation at the microscale in fiber-reinforced composites. *Compos Part A-Appl S*, 43(10):1630–1638, 2012.
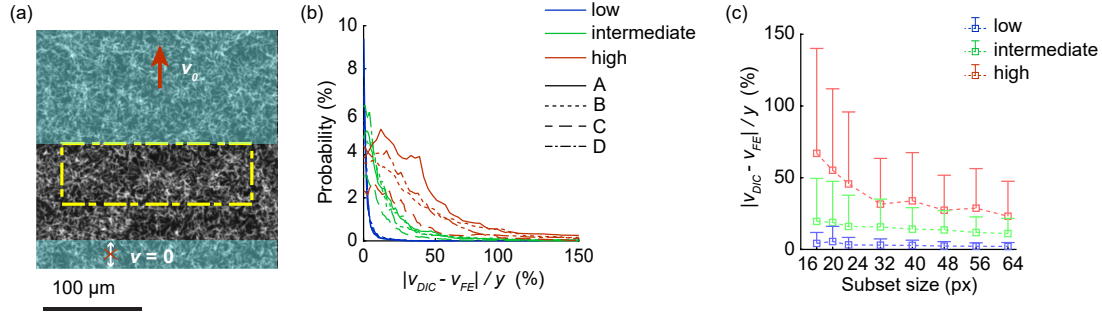
Figure 11: Deformation in uniaxial extension. (a) Boundary conditions used. Nodes near the bottom of the fiber network were constrained to have zero displacement in the y direction; nodes at the top were translated in the y direction. The dashed rectangle shows the ROI. (b) Distribution of errors in the ROI in FIDIC estimates of normalized displacement, v/y, (subset size, 32×32 px; subset spacing, 8 px). Colors show levels of applied strain and line types indicate the network being considered. (c) Errors in FIDIC estimates for several different subset sizes at low ($\approx 2\%$), intermediate ($\approx 20\%$) and high ($\approx 60\%$) magnitudes of strain for representative network C. The subset spacing was a quarter of the subset size for all cases.

[4] G Subhash, Q Liu, DF Moore, PG Ifju, and MA Haile. Concentration dependence of tensile behavior in agarose gel using digital image correlation. *Exp Mech*, 51(2):255–262, 2011.

[5] Peng Wang, F Pierron, and Ole Thybo Thomsen. Identification of material parameters of pvc foams using digital image correlation and the virtual fields method. *Exp Mech*, 53(6):1001–1015, 2013.

[6] Tahreer M Fayyad and Janet M Lees. Application of digital image correlation to reinforced concrete fracture. *Proc Mat Sci*, 3:1585–1590, 2014.

[7] MA Tschopp, BB Bartha, WJ Porter, PT Murray, and SB Fairchild. Microstructure-dependent local strain behavior in polycrystals through in-situ scanning electron microscope tensile experiments. *Metall Mater Trans A*, 40(10):2363–2368, 2009.

[8] Samer Sadek, Magued G Iskander, and Jinyuan Liu. Accuracy of digital image correlation for measuring deformations in transparent media. *J Comput Civil Eng*, 17(2):88–96, 2003.

[9] Brian K Bay, Tait S Smith, David P Fyhrie, and Malik Saad. Digital volume correlation: three-dimensional strain mapping using X-ray tomography. *Exp Mech*, 39(3):217–226, 1999.

[10] Eelco Verhulp, Bert van Rietbergen, and Rik Huiskes. A three-dimensional digital image correlation technique for strain measurements in microstructures. *J Biomech*, 37(9):1313–1320, 2004.

[11] R Zauel, YN Yeni, BK Bay, XN Dong, and David P Fyhrie. Comparison of the linear finite element prediction of deformation and strain of human cancellous bone to 3d digital volume correlation measurements. *J Biomech Eng—T ASME*, 128(1):1–6, 2006.

[12] Blayne A Roeder, Klod Kokini, J Paul Robinson, and Sherry L Voytik-Harbin. Local, three-dimensional strain measurements within largely deformed extracellular matrix constructs. *J Biomech Eng—T ASME*, 126(6):699–708, 2004.

[13] Ruoya Wang, Luke P Brewster, and Rudolph L Gleason Jr. In-situ characterization of the uncrimping process of arterial collagen fibers using two-photon confocal microscopy and digital image correlation. *J Biomech*, 46(15):2726–2729, 2013.

[14] Jacob Notbohm, Ayelet Lesman, David A Tirrell, and Guruswami Ravichandran. Quantifying cell-induced matrix deformation in three dimensions based on imaging matrix fibers. *Integr Biol*, 7(10):1186–1195, 2015.

[15] Jihan Kim, Christopher AR Jones, Nicholas Scott Groves, and Bo Sun. Three-dimensional reflectance traction microscopy. *Plos One*, 11(6):e0156797, 2016.

[16] Leanna M Owen, Arjun S Adhikari, Mohak Patel, Peter Grimmer, Natascha Leijnse, Min Cheol Kim, Jacob Notbohm, Christian Franck, and Alexander R Dunn. A cytoskeletal clutch mediates cellular force transmission in a soft, three-dimensional extracellular matrix. *Mol Biol Cell*, 28(14):1959–1974, 2017.

[17] Brian Burkel and Jacob Notbohm. Mechanical response of collagen networks to nonuniform microscale loads. *Soft Matter*, 13(34):5749–5758, 2017.

[18] Sébastien Leprince, François Ayoub, Yann Klinger, and Jean-Philippe Avouac. Co-registration of optically sensed images and correlation (cosi-corr): An operational methodology for ground deformation measurements. In *2007 IEEE International Geoscience and Remote Sensing Symposium*, pages 1943–1946. IEEE, 2007.

[19] Paolo Caporossi, Paolo Mazzanti, and Francesca Bozzano. Digital image correlation (DIC) analysis of the 3 December 2013 Montescaglioso landslide (Basilicata, southern Italy): results from a multi-dataset investigation. *ISPRS Int J Geo-Inf*, 7(9):372, 2018.

[20] Paolo Mazzanti, Paolo Caporossi, and Riccardo Muzi. Sliding time master digital image correlation analyses of cubesat images for landslide monitoring: The rattlesnake hills landslide (USA). *Remote Sens*, 12(4):592, 2020.

[21] Bing Pan, Bo Wang, Gilles Lubineau, and Ali Moussawi. Comparison of subset-based local and finite element-based global digital image correlation. *Exp Mech*, 55(5):887–901, 2015.

[22] BA DiDonna and TC Lubensky. Nonaffine correlations in random elastic media. *Phys Rev E*, 72(6):066619, 2005.

[23] DA Head, AJ Levine, and FC MacKintosh. Distinct regimes of elastic response and deformation modes of cross-linked cytoskeletal and semiflexible polymer networks. *Phys Rev E*, 68(6):061907, 2003.

[24] DA Head, AJ Levine, and FC MacKintosh. Mechanical response of semiflexible networks to localized perturbations. *Phys Rev E*, 72(6):061914, 2005.

[25] Preethi L Chandran and Victor H Barocas. Affine versus non-affine fibril kinematics in collagen networks: theoretical studies of network behavior. *J Biomech Eng—T ASME*, 128(2):259–270, 2006.

[26] H Hatami-Marbini and RC Picu. Scaling of nonaffine deformation in random semiflexible fiber networks. *Phys Rev E*, 77(6):062103, 2008.

[27] Peter Grimmer and Jacob Notbohm. Displacement propagation in fibrous networks due to local contraction. *J Biomech Eng—T ASME*, 140(4):041011, 2018.

[28] Jingchen Feng, Herbert Levine, Xiaoming Mao, and Leonard M Sander. Alignment and nonlinear elasticity in biopolymer gels. *Phys Rev E*, 91(4):042710, 2015.

[29] Albert James Licup, Stefan Münster, Abhinav Sharma, Michael Sheinman, Louise M Jawerth, Ben Fabry, David A Weitz, and Fred C MacKintosh. Stress controls the mechanics of collagen networks. *P Nat Acad Sci USA*, 112(31):9573–9578, 2015.

[30] Mahsa Vahabi, Abhinav Sharma, Albert James Licup, Anne SG Van Oosten, Peter A Galie, Paul A Janmey, and Fred C MacKintosh. Elasticity of fibrous networks under uniaxial prestress. *Soft Matter*, 12(22):5050–5060, 2016.

[31] Anne SG Van Oosten, Mahsa Vahabi, Albert J Licup, Abhinav Sharma, Peter A Galie, Fred C MacKintosh, and Paul A Janmey. Uncoupling shear and uniaxial elastic moduli of semiflexible biopolymer networks: compression-softening and stretch-stiffening. *Sci Rep-UK*, 6(1):19270, 2016.

[32] KL Billiar and MS Sacks. A method to quantify the fiber kinematics of planar tissues under biaxial stretch. *J Biomech*, 30(7):753–756, 1997.

[33] Qi Wen, Anindita Basu, Jessamine P Winer, Arjun Yodh, and Paul A Janmey. Local and global deformations in a strain-stiffening fibrin gel. *New J Phys*, 9(11):428, 2007.

[34] J Liu, GH Koenderink, KE Kasza, FC MacKintosh, and DA Weitz. Visualizing the strain field in semiflexible polymer networks: strain fluctuations and nonlinear rheology of F-actin gels. *Phys Rev Lett*, 98(19):198304, 2007.

[35] Tobias T Falzone and Rae M Robertson-Anderson. Active entanglement-tracking microrheology directly couples macromolecular deformations to nonlinear microscale force response of entangled actin. *ACS Macro Lett*, 4(11):1194–1199, 2015.

[36] Brian Burkel, Maria Proestaki, Stephen Tyznik, and Jacob Notbohm. Heterogeneity and nonaffinity of cell-induced matrix displacements. *Phys Rev E*, 98(5):052410, 2018.

[37] Hubert W Schreier and Michael A Sutton. Systematic errors in digital image correlation due to undermatched subset shape functions. *Exp Mech*, 42(3):303–310, 2002.

[38] Marina Fazzini, Sébastien Mistou, Olivier Dalverny, and Laurent Robert. Study of image characteristics on digital image correlation error assessment. *Opt Laser Eng*, 48(3):335–339, 2010.

[39] Stefan B Lindström, David A Vader, Artem Kulachenko, and David A Weitz. Biopolymer network geometries: Characterization, regeneration, and elastic properties. *Phys Rev E*, 82(5):051905, 2010.

[40] Stefan B Lindström, Artem Kulachenko, Louise M Jawerth, and David A Vader. Finite-strain, finite-size mechanics of rigidly cross-linked biopolymer networks. *Soft Matter*, 9(30):7302–7313, 2013.

[41] PR Onck, T Koeman, T Van Dillen, and Erik van der Giessen. Alternative explanation of stiffening in cross-linked semiflexible networks. *Phys Rev Lett*, 95(17):178102, 2005.

[42] Cornelis Storm, Jennifer J Pastore, Fred C MacKintosh, Tom C Lubensky, and Paul A Janmey. Nonlinear elasticity in biological gels. *Nature*, 435(7039):191–194, 2005.

[43] Maria Proestaki, Brian Burkel, Emmett E Galles, Suzanne M Ponik, and Jacob Notbohm. Effect of matrix heterogeneity on cell mechanosensing. *Soft Matter*, (17):10263–10273, 2021.

[44] Sven K Esche, Gary L Kinzel, and Taylan Altan. Issues in convergence improvement for non-linear finite element programs. *Int J Numer Meth Eng*, 40(24):4577–4594, 1997.

[45] William C. Warger II, Charles A. DiMarzio, and Milind Rajadhyaksha. Chapter 25: Confocal microscopy. In *Handbook of Biomedical Optics*, pages 517–541. CRC press, Boca Raton, FL, 2016.

[46] Max Born and Emil Wolf. *Principles of optics: electromagnetic theory of propagation, interference and diffraction of light*. Pergamon, New York, 1980.

[47] Yajie Xing, Jingbo Wang, Xiaokang Chen, and Gang Zeng. 2.5 D convolution for RGB-D semantic segmentation. *IEEE Image Proc*, pages 1410–1414, 2019.

[48] James B Pawley. Sources of noise in three-dimensional microscopical data sets. In *Three-Dimensional Confocal Microscopy: Volume Investigation of Biological Specimens*, pages 47–94. Academic Press, New York, 1994.

[49] Zikuan Chen and Ruola Ning. Three-dimensional point spread function measurement of cone-beam computed tomography system by iterative edge-blurring algorithm. *Phys Med Biol*, 49(10):1865, 2004.

[50] Peter J Creveling, William W Whitacre, and Michael W Czabaj. A fiber-segmentation algorithm for composites imaged using x-ray microtomography: Development and validation. *Compos Part A-Appl S*, 126:105606, 2019.

[51] Erik LG Wernersson, Cris L Luengo Hendriks, and Anders Brun. Generating synthetic μct images of wood fibre materials. In *2009 Proceedings of 6th International Symposium on Image and Signal Processing and Analysis*, pages 365–370. IEEE, 2009.

[52] Zeinab Khorrami, Pouria Khalaj, Anne SM Buckner, Paul C Clark, Estelle Moraux, Stuart Lumsden, Isabelle Joncour, René D Oudmaijer, Ignacio de la Calle, José M Herrera-Fernandez, et al. A code to make your own synthetic observations (myosotis). *Mon Not R Astron Soc*, 485(3):3124–3133, 2019.

[53] Michele Badaloni, Marco Rossi, Gianluca Chiappini, Pascal Lava, and Dimitri Debruyne. Impact of experimental uncertainties on the identification of mechanical material properties using dic. *Exp Mech*, 55(8):1411–1426, 2015.

[54] E Bar-Kochba, J Toyjanova, E Andrews, K-S Kim, and Christian Franck. A fast iterative digital volume correlation algorithm for large deformations. *Exp Mech*, 55(1):261–274, 2015.

[55] Joseph M Szulczewski, David R Inman, Maria Proestaki, Jacob Notbohm, Brian M Burkel, and Suzanne M Ponik. Directional cues in the tumor microenvironment due to cell contraction against aligned collagen fibers. *Acta Biomater*, 129:96–109, 2021.

[56] J Yang and K Bhattacharya. Augmented lagrangian digital image correlation. *Exp Mech*, 59(2):187–205, 2019.

[57] J Nogueira, A Lecuona, PA Rodriguez, JA Alfaro, and A Acosta. Limits on the resolution of correlation piv iterative methods. practical implementation and design of weighting functions. *Exp Fluids*, 39(2):314–321, 2005.

[58] Michel Bornert, Fabrice Brémand, Pascal Doumalin, J-C Dupré, Marina Fazzini, M Grédiac, François Hild, Sebastien Mistou, Jérôme Molimard, J-J Orteu, et al. Assessment of digital image correlation measurement errors: methodology and results. *Exp Mech*, 49(3):353–370, 2009.

[59] Elizabeth MC Jones and Mark A) Iadicola. A good practices guide for digital image correlation. *International Digital Image Correlation Society*, 10, 2018.

[60] Jacob Notbohm, Ayelet Lesman, Phoebus Rosakis, David A Tirrell, and Guruswami Ravichandran. Microbuckling of fibrin provides a mechanism for cell mechanosensing. *J R Soc Interface*, 12(108):20150320, 2015.

[61] Mathilda S Rudnicki, Heather A Cirka, Maziar Aghvami, Edward A Sander, Qi Wen, and Kristen L Billiar. Nonlinear strain stiffening is not sufficient to explain how far cells can feel on fibrous protein gels. *Biophys J*, 105(1):11–20, 2013.

[62] Hailong Wang, AS Abhilash, Christopher S Chen, Rebecca G Wells, and Vivek B Shenoy. Long-range force transmission in fibrous matrices enabled by tension-driven alignment of fibers. *Biophys J*, 107(11):2592–2603, 2014.

[63] Phoebus Rosakis, Jacob Notbohm, and Guruswami Ravichandran. A model for compression-weakening materials and the elastic fields due to contractile cells. *J Mech Phys Solids*, 85:16–32, 2015.

[64] Ali Rouwane, Robin Bouclier, Jean-Charles Passieux, and Jean-Noël Périé. Architecture-driven digital image correlation technique (ADDICT) for the measurement of sub-cellular kinematic fields in speckle-free cellular materials. *Int J Solids Struct*, 234:111223, 2022.

[65] SM Kleinendorst, JPM Hoefnagels, and MGD Geers. Mechanical shape correlation: A novel integrated digital image correlation approach. *Comput Method Appl M*, 345:983–1006, 2019.